

# Oscillatory surface rheotaxis of swimming *E. coli* bacteria

Arnold J. T. M. Mathijssen,<sup>1</sup> Nuris Figueroa-Morales,<sup>2,\*</sup> Gaspard

Junot,<sup>3</sup> Éric Clément,<sup>3</sup> Anke Lindner,<sup>3</sup> and Andreas Zöttl<sup>4,†</sup>

<sup>1</sup>*Department of Bioengineering, Stanford University,  
443 Via Ortega, Stanford, CA 94305, USA*

<sup>2</sup>*Department of Biomedical Engineering,  
Penn State University, University Park, PA 16802, USA*

<sup>3</sup>*PMMH, UMR 7636 CNRS-ESPCI-Universités Pierre et Marie Curie and Denis Diderot,  
10, rue Vauquelin, 75231 Paris Cedex 5, France*

<sup>4</sup>*Rudolf Peierls Centre for Theoretical Physics,  
University of Oxford, 1 Keble Road, OX1 3NP, UK*

(Dated: December 14, 2024)

## Abstract

We demonstrate experimentally and theoretically the existence of oscillatory rheotaxis by *E. coli* bacteria swimming at surfaces under flow. Three transitions are identified with increasing shear rate: From circular to straight upstream motion, the emergence of oscillations, and finally coexistence of rheotaxis along the positive and negative vorticity directions. We develop a model to explain these transitions and predict the corresponding critical shear rates. Our results shed new light on bacterial transport in the presence of confining walls and strategies for contamination prevention.

---

\* Present address: Department of Biomedical Engineering, Penn State University, 508 Wartik Lab, PA 16802, USA

† andreas.zoettl@physics.ox.ac.uk

*Introduction* Swimming microorganisms respond to flows in highly diverse and complex environments, at scales ranging from open oceans to narrow capillaries [1–3]. To succeed in such diverse conditions, microbial transport often features surprising dynamics. Microswimmers can accumulate in shear flows [4–7], swim along the vorticity direction [8], exhibit oscillatory trajectories and upstream motion in Poiseuille flows [6, 9], or align resonantly in oscillatory flows [10]. These individual observations were explained separately by accounting for hydrodynamics and/or the swimmers’ complex shape [6, 9, 11–14]. Together, however, the interplay of these properties remains largely unexplored.

Moreover, in the presence of walls these dynamics become increasingly intricate [15–18], but due to boundary accumulation [19–21] the understanding of surface locomotion is of particular importance. Due to their body rotation flagellated micro-swimmers move in circles in quiescent liquids [22–24], but in flows they can orient with respect to the flow direction and velocity gradients. The robustness of upstream swimming attributed to fore-aft asymmetry of the swimmer shape was analysed theoretically [25–27], and observed for artificial microswimmers [28], sperm cells [29, 30] and *E. coli* bacteria [31–34]. Yet, at higher flow rates *E. coli* orient transversally, “to the right”, along the vorticity direction [31–33]. This effect, baptized “rheotaxis”, is attributed to inherent flagellar chirality and has first been observed for sperm cells [35]. Predictions for this transition from upstream to transversal rheotaxis for bacteria are actively sought after. To date, bacterial rheotaxis at surfaces has been quantified by measuring instantaneous orientation distributions [31] or average transport velocities [33], but a complete picture of the surface dynamics is still missing.

Here, we investigate, for the first time, the time-resolved orientation dynamics of *E. coli* bacteria, theoretically and experimentally, as a function of applied shear close to walls. With increasing flow, we identify four regimes separated by critical shear rates: (*I*) circular swimming with a bias along the direction of vorticity; (*II*) upstream swimming without oscillations; (*III*) oscillatory motion, increasingly more to the right; (*IV*) coexistence of swimming to the right and to the left, with dynamical switching between these states. By modeling bacterial rheotaxis comprehensively – accounting for their chiral nature, hydrodynamic and steric interactions, elongation, fore-aft asymmetry and activity – we assess the relative importance of these contributions throughout a trajectory, and explain the full dynamics.

*Experimental observations* We observe the dynamics of non-tumbling *E. coli* bacteria at surfaces under flow (see Fig. 1(a) and Supplemental Material (SM) §1 [36]). A 3D tracking technique [37] provides bacteria trajectories at distances from the bottom surface of up to  $5\text{ }\mu\text{m}$ . Typical trajectories are shown on Fig. 1(b) in the laboratory frame for wall shear rates  $\dot{\gamma} = 1 - 50\text{s}^{-1}$ . Here  $\dot{\gamma} = \frac{4V_{\text{max}}}{H}$ , where  $V_{\text{max}}$  is the maximum flow velocity and  $H$  is the channel height. With increasing shear rate very different trajectories are observed. At small shear rates the well-known circular motion [22–24] starts to evolve towards cycloid motion with a bias to the right. Eventually, circles become suppressed and upstream motion can be observed. When further increasing the shear rate bacteria are transported downstream more strongly and the laboratory frame trajectories bend into the direction of the flow. These trajectories are mostly oriented towards the right [31], but we observe for the first time

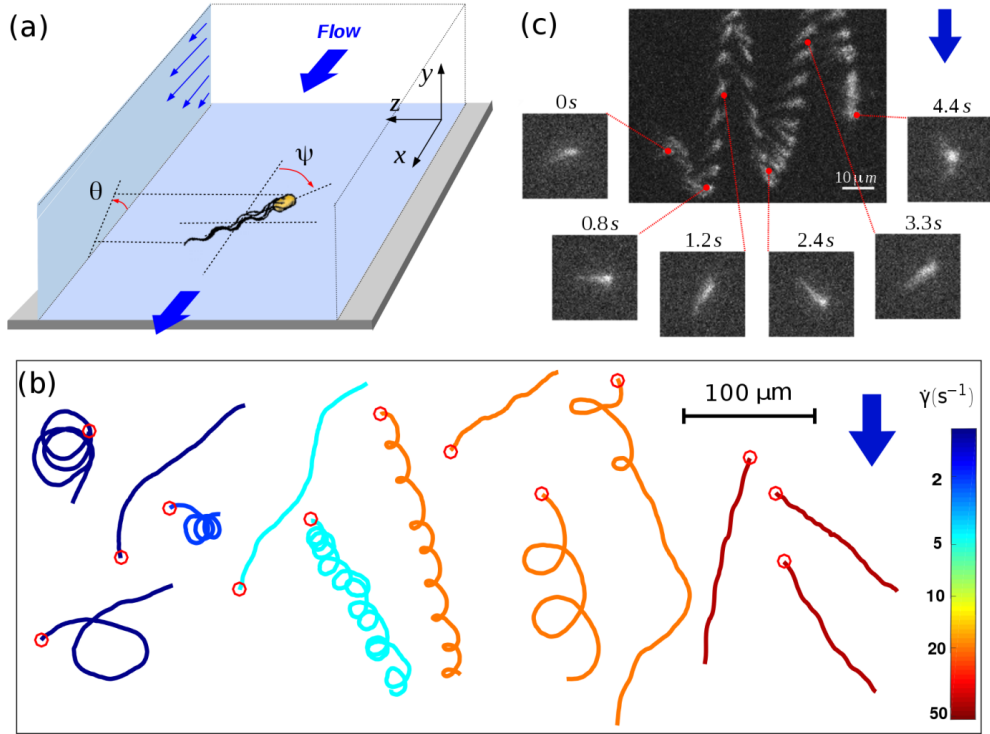


FIG. 1. Experimental observation of oscillatory rheotaxis. (a) Set-up geometry. (b) Various surface trajectory types obtained from 3D tracking at shear rates  $\dot{\gamma} = 1 - 50\text{s}^{-1}$  shown in the lab frame at a distance  $2\text{--}5\text{ }\mu\text{m}$  from the bottom surface. (c) Time lapse of an oscillating bacterium with fluorescently stained flagella, using 10 fps snapshots overlaid to highlight its trajectory, and taken in the Lagrangian reference frame of the average downstream bacterial velocity at  $\dot{\gamma} = 78\text{s}^{-1}$ .

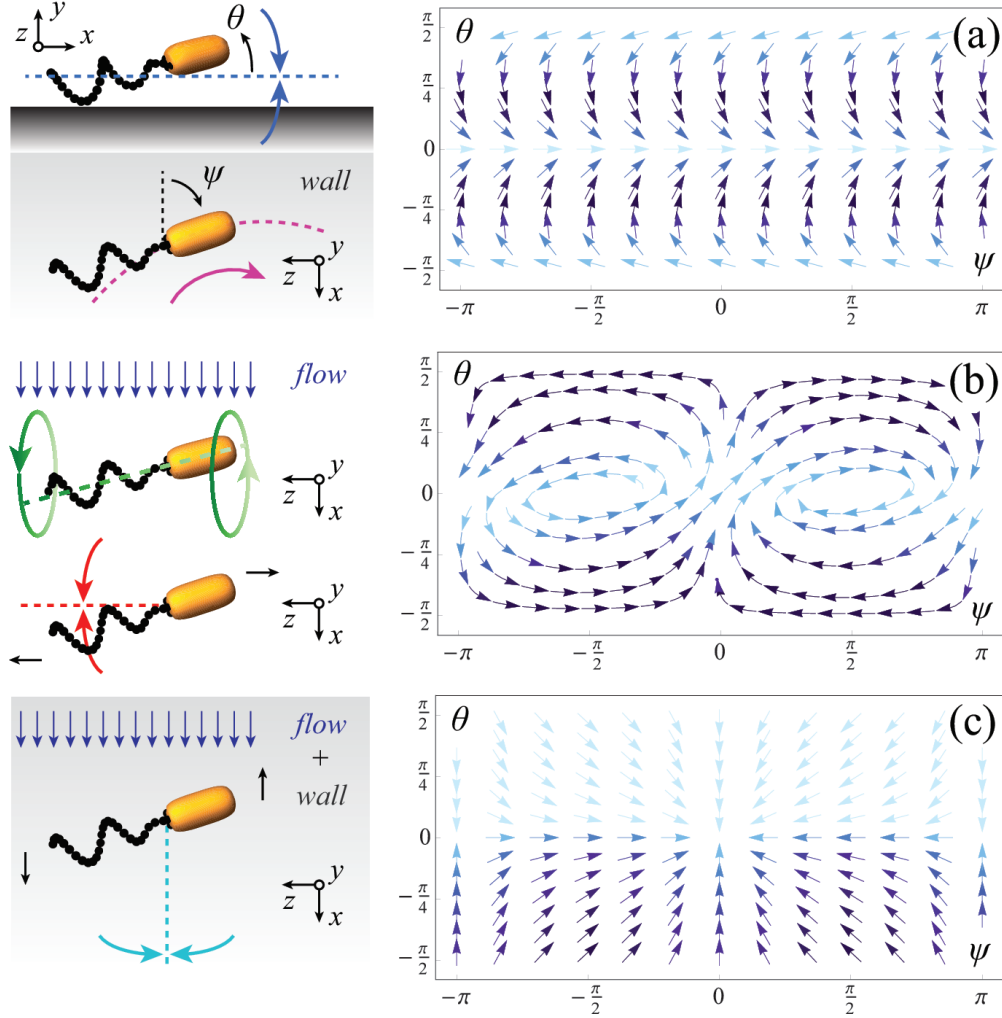


FIG. 2. Summary of terms included in the model (left), and the corresponding orientation dynamics (right). (a) Wall interactions align swimmers with walls (blue). Clock-wise swimming in circles (pink). (b) Jeffery orbits of elongated bacteria (green). Helix in shear reorients swimmers to the right (red). (c) Weathervane effect reorients swimmers to the upstream direction (cyan).

that swimming towards the left can also occur. On some of these trajectories an oscillatory motion appears. This can be seen more clearly on complementary experiments performed on bacteria with fluorescently labeled body and flagella, where bacteria orientation can be directly visualised. While some bacteria swim at a stable angle we have identified novel oscillations between the upstream- and downstream orientations, as shown in Fig. 1(b). Note also that for a given experimental condition, different types of trajectories may coexist, most likely due to the sensitivity of trajectories to slight variations in the distance from the wall, variations in bacterial shape, and other sources of noise inherent to the swimming of living

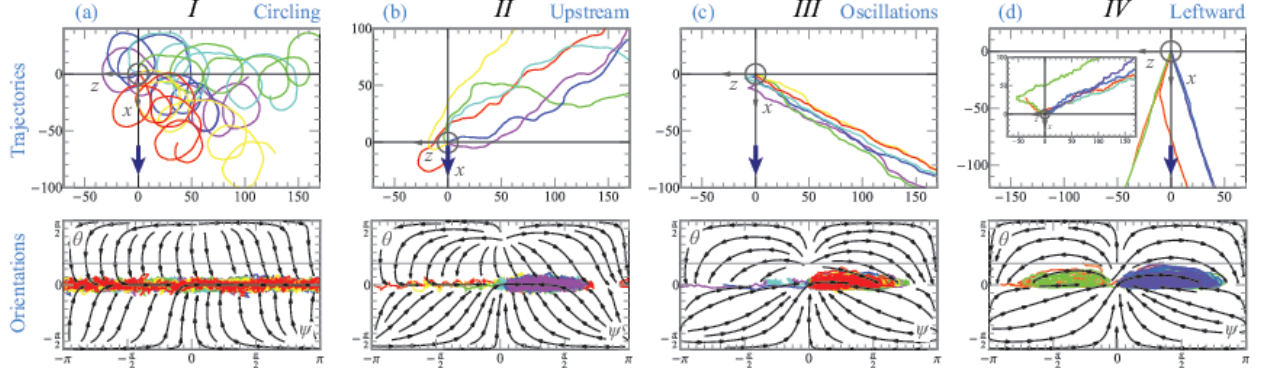


FIG. 3. Simulated trajectories of surface rheotaxis (upper panels) in the laboratory frame and the corresponding orientation dynamics (lower panels) in the four different regimes with increasing shear rate: (I,  $\dot{\gamma} = 1\text{s}^{-1}$ ) Circular swimming with a bias to the right. (II,  $\dot{\gamma} = 5\text{s}^{-1}$ ) Upstream motion. (III,  $\dot{\gamma} = 20\text{s}^{-1}$ ) Oscillatory motion, increasingly more to the right. (IV,  $\dot{\gamma} = 50\text{s}^{-1}$ ) Coexistence between swimming to the right and to the left, with dynamical switching between these. Grey circles indicate the initial swimmer positions. Parameters:  $\Gamma = 5$ ,  $\nu_W = 3\text{s}^{-1}$ ,  $\nu_D = 0.5\text{s}^{-1}$ ,  $\bar{\nu}_H = 0.02$ ,  $\bar{\nu}_V = 0.75$ ,  $\theta_V = 0.04$ ,  $\theta_e = \pi/6$ ,  $v_s = 20\mu\text{ms}^{-1}$ ,  $h_s = 0.5\mu\text{m}$ ,  $D_r = 0.057\text{s}^{-1}$ .

bacteria.

*Model* In order to understand the rich behavior of our experimental findings, we model a bacterium subject to shear flow of shear rate  $\dot{\gamma}$  at a surface [Fig. 2]. Attached to its elongated body – length  $L$ , width  $W$ , and aspect ratio  $\Gamma = L/W$  – is a stiff left-handed (normal form) helical flagellar bundle. Its in-plane angle is  $\psi \in \{-\pi, \pi\}$  and  $\theta \in \{-\pi/2, \pi/2\}$  is the dipping angle [Fig. 1(a)]. Note, the bacterial conformation in principle also depends on the helix phase angle, but we average over it owing to the fast flagellar rotation. After a swimmer has reached the surface, its orientation evolves as

$$\dot{\psi} = \Omega_\psi(\psi, \theta), \quad \dot{\theta} = \Omega_\theta(\psi, \theta), \quad (1)$$

where the reorientation rates  $\Omega_\psi$  and  $\Omega_\theta$  stem from three main contributions,  $\Omega = \Omega^W + \Omega^F + \Omega^V$ , that account for the presence of the wall ( $\Omega^W$ ), local shear flow ( $\Omega^F$ ), and surface-flow coupled effects ( $\Omega^V$ ).

First, in the absence of flow, hydrodynamic swimmer-wall interactions [20, 38] and steric interactions [21] enable bacteria to swim at a stable orientation approximately parallel to

the wall [39–42]. We model this surface alignment as [38]

$$\Omega_\theta^W(\theta) = -\nu_W \sin 2\theta \left( 1 + \frac{G}{2}(1 + \cos^2 \theta) \right), \quad (2)$$

where  $G = (\Gamma^2 - 1)/(\Gamma^2 + 1) \lesssim 1$ . Here the prefactor  $\nu_W$  is an effective angular rate capturing both the hydrodynamic and steric contributions (see also SM §4b [36]). The counter-rotation of the head and flagellar bundle leads to a clockwise rotation of the bacterial trajectories at solid surfaces [24, 39]. The associated reorientation rate in the  $\psi$  direction is approximated (see [38]) by

$$\Omega_\psi^W(\theta) = \nu_C(1 - 3 \sin^2 \theta + G \cos^2 \theta(1 + 3 \sin^2 \theta)), \quad (3)$$

where  $\nu_C > 0$  can be estimated from experiments [24]. The combined wall-induced effects from (2) and (3) are shown in Fig. 2(a). After a swimmer reaches the surface with  $\theta < 0$  it quickly reorients parallel to it and swims in circles, meaning a constant increase of the angle  $\psi$ .

Second, we discuss the effect of shear flows. Elongated objects such as rods and fibers, or dead bacteria [43], perform Jefferey orbits [44] such that the orientation vector performs a periodic motion given by

$$\begin{aligned} \Omega_\psi^J &= \frac{\dot{\gamma}}{2}(1 + G) \sin \psi \tan \theta, \\ \Omega_\theta^J &= \frac{\dot{\gamma}}{2}(1 - G \cos 2\theta) \cos \psi. \end{aligned} \quad (4)$$

Note, we assume that the presence of the wall does not significantly modify the reorientation rates, in accordance with previous observations [45]. However, particle chirality (in addition to activity) enables stream-line crossing [14, 46], which in the bulk leads to a net migration of bacteria [8]. Based on the calculations in Ref. [8], we account for this effect using resistive force theory (RFT) applied to a helical flagella bundle under shear flow (see SM §2 [36]). This yields the chirality-induced reorientation rates

$$\begin{aligned} \Omega_\psi^H &= \dot{\gamma} \bar{\nu}_H \cos \psi \frac{\cos 2\theta}{\cos \theta}, \\ \Omega_\theta^H &= \dot{\gamma} \bar{\nu}_H \sin \psi \sin \theta. \end{aligned} \quad (5)$$

with  $\bar{\nu}_H \ll 1$  (see also SM §4d [36]). Interestingly, the combined effects of Jefferey orbits (4) and chirality (5) give rise to a stable ‘spiral’ fixed point in orientation space [Fig. 2(b)], breaking symmetry ‘to the right’.

Third, we introduce a term that has been identified as an important contribution for sperm rheotaxis [29, 30]. The swimmer body experiences an effective *anchoring* to the surface when pointing towards it because its hydrodynamic friction with the wall is larger than the flagellar bundle, an effect explained by lubrication theory [30]. Consequently, the flagella are advected with the flow, like a *weathervane*, such that the bacteria orients upstream [29, 30, 47],

$$\Omega_{\alpha}^V = -\dot{\gamma}\bar{\nu}_V \sin(\alpha) \left[ \frac{1}{2} \left( 1 - \tanh \frac{\theta}{\theta_V} \right) \right], \quad (6)$$

for both  $\alpha = \{\theta, \psi\}$ . The hyperbolic tangent, with constant small  $\theta_V$ , accounts for the fact that the asymmetry in friction reduces when the swimmer faces away from the surface,  $\theta > 0$ , where the weathervane effect disappears [Fig. 2(c)]. This notion was not included in the single-angle descriptions used for sperm [29, 30].

Finally, we solve the orientation dynamics by integrating Eqs. (1), combining the aforementioned contributions together with rotational noise ( $D_r = 0.057\text{s}^{-1}$  [48]), without tumbling, as detailed in SM §3 [36]. A trajectory starts with a random  $\psi$  and a slightly negative  $\theta$ , but finishes when it reaches a given escape angle  $\theta_e$  [48–50]. Subsequently, the spatial dynamics are found by computing the velocity parallel to the surface, at speed  $v_s$ , including downstream advection at distance  $y = h_s$ .

*Model results* Figure 3 shows typical trajectories and the orientation dynamics in  $\psi$ - $\theta$  space for different shear rates  $\dot{\gamma}$  and initial conditions. These results are qualitatively robust for changes in parameters, but the values chosen here have been estimated from experiments and numerical models (see SM §4 [36]). We identify four regimes (*I-IV*) separated by critical shear rates:

At weak flows (regime *I*) the bacteria move in circular trajectories, with a drift to the right [Fig. 3(a)]. Above a critical shear rate,  $\dot{\gamma}_{c_1} = 2(G + 1)\nu_{DR}/\bar{\nu}_V \sim 2.6\text{s}^{-1}$ , derived in SM §5b [36], they break out of the circles and swim stable to the right (regime *II*). This so-called Adler transition has also been observed for sperm cells [30], and stems from the competition between the rotation (3) and the weathervane effect (6) that increases with flow. This is described by the in-plane angle only:  $\psi$  decreases with increasing  $\dot{\gamma}$  so that the cells orient more upstream [Fig. 3(b) & Fig. 4(a); green lines]. Owing to noise, coexistence between circling and stable swimming may exist close to  $\dot{\gamma}_{c_1}$ , and oscillations may also appear already, as discussed below.

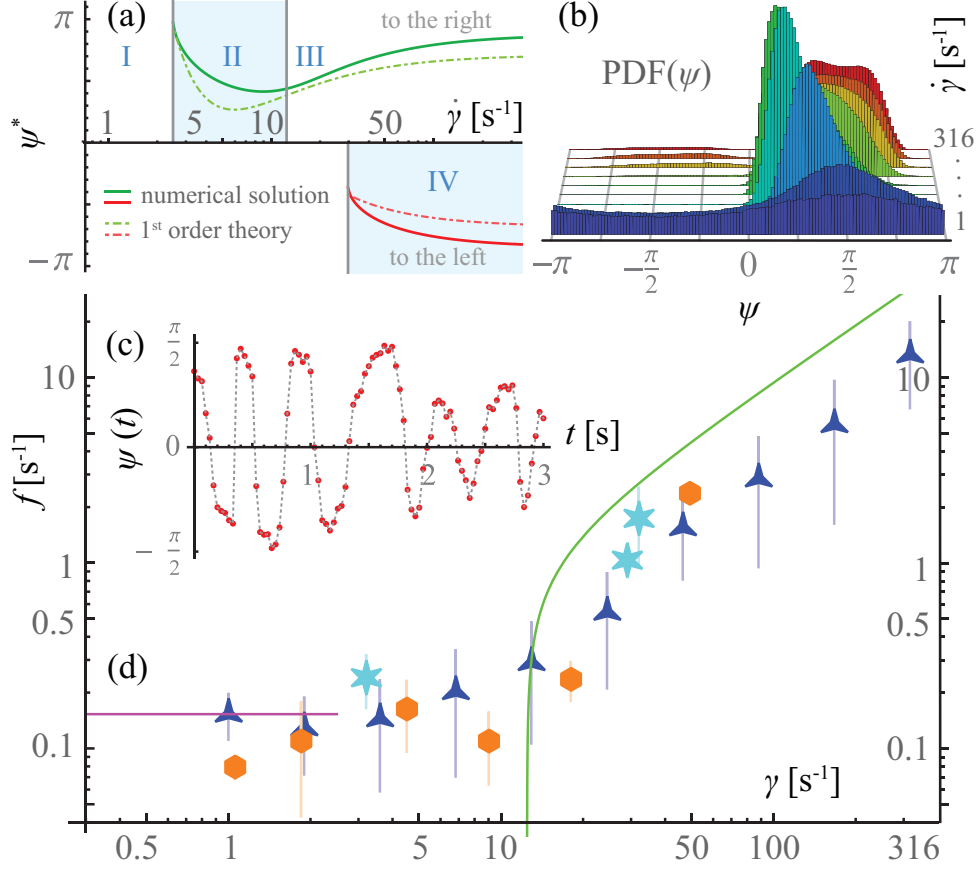


FIG. 4. Bacterial orientation as a function of applied shear. Parameters used are the same as in Fig. 3. (a) Equilibrium in-plane angle  $\psi$ , obtained numerically (solid lines) and analytically (dashed lines), with critical shear rates (grey lines). (b) Steady-state distribution of  $\psi$ , obtained by simulating  $N = 10^4$  trajectories at each shear rate. (c) Typical temporal evolution of  $\psi(t)$  from a fluorescence experiment at  $\dot{\gamma} = 33\text{s}^{-1}$ . (d) Oscillation frequency versus shear rate, obtained from Fourier transformation of  $v_z(t)$  in 3D tracking experiments (orange hexagons), and of  $\psi(t)$  in both fluorescence experiments (cyan stars) and simulations (blue triangles); Theoretical estimates from linearisation (green line) and the circling frequency,  $\Omega_\psi^W(\theta=0)/2\pi$ , (magenta line).

Above a second critical shear rate,  $\dot{\gamma}_{c2} \sim 13\text{s}^{-1}$  (regime *III*), an oscillatory motion emerges [Fig. 3(c)] that can be envisaged as a 4-step process: (1) The flow slightly lifts the head of an upstream-oriented bacterium from the surface, thus  $\theta$  increases according to the Jefferey term. (2) Then the weathervane effect diminishes so that the swimmer rotates away from the upstream direction, rightwards or leftwards, increasing  $|\psi|$ . (3) Once the bacterium is oriented downstream, the flow pushes its head down onto the surface so that  $\theta$  decreases. (4)



Therefore the weathervane effect turns on again, leading once more to upstream orientations and the cycle is repeated.

Moreover, in regimes *II-III* the average orientation  $\psi^*$  shifts from upstream swimming ( $\psi = 0$ ) to the right ( $\psi > 0$ ) [Fig. 4(a); green lines], in agreement with previous studies [31–33]. This is explained by the weakening of the weathervane effect (6), which induces upstream motion, because the surface anchoring is reduced by the Jeffery term (4) that tries to rotate the bacterium away from the surface ( $\theta > 0$ ) [see also Fig. 2(b)]. Consequently, the optimal shear rate for upstream orientation is given by the minimum in  $\psi(\dot{\gamma})$ , computed in SM §5d [36].

Above a third critical shear rate,  $\dot{\gamma}_{c3} \sim 30\text{s}^{-1}$  (regime *IV*), the possibility of oscillatory swimming to the left emerges,  $\psi \sim -\pi/2$  [Fig. 4(a); red lines], in coexistence with the aforementioned rightward motion [green lines]. Also, bacteria may switch dynamically between the left and right [Fig. 3(d); orange and green trajectories]. However, this mode of rheotaxis is rare, as the fraction of bacteria oriented to the left is only  $\sim 4\%$  at large shear rates [Fig. 4(b)], and hence the bacterial motion remains biased to the right.

All types of trajectories predicted by our model have also been observed experimentally [Fig. 1(b)]. Visual differences arise from fluctuations, and distance variations with respect to the wall. Experimentally, bacteria trajectories are taken into account for distances up to  $5\mu\text{m}$  from the surface, yielding a variability in the advection velocities, and hence affecting the visual aspect of the trajectories in the laboratory reference frame. The angular dynamics of the rheotaxis, however, are very well captured. In particular, the oscillation frequencies obtained from Fourier transformation of the experimental trajectories [see e.g. Fig. 4(c)] match the simulated frequencies quantitatively [Fig. 4(d)].

Furthermore, analytical progress can be made in the absence of noise, when oscillations are damped by wall alignment so that trajectories end at a stable position in  $(\psi, \theta)$  space. This equilibrium orientation can be found numerically from the fixed points of Eq. 1 [Fig. 4(a); solid lines] or estimated analytically (see SM §5c [36]) by linearising Eq. (1) about  $(\psi, \theta) = (\pm\pi/2, 0)$  and solving for the two fixed points [Fig. 4(a); dashed lines]. This solution agrees well with the simulated steady-state distribution of orientation angles [Fig. 4(b)], featuring peaks around the equilibrium angle(s). Furthermore, linearising around the fixed points also gives formulae (see SM §5e [36]) for the second critical shear rate and the oscillation frequency [Fig. 4(d); green line], again in agreement with the experimental values.

However, fluctuations do have three main effects: First, they sustain oscillations despite the wall-alignment damping, as observed in experiments [Fig. 1(c)] and simulations with noise [Fig. 3(c-d)]. Second, they also allow for oscillations to emerge below the critical shear  $\dot{\gamma}_{c2}$ , as seen in Fig. 3(b) and Fig. 4(d). Third, they facilitate dynamical switching between left and right-orientated rheotaxis [Fig. 3(d)]. Indeed, bacterial tumble events will additionally contribute to these oscillations and switches. For wild-type strains the average population dynamics at surfaces is expected to depend quite sensibly on the run-time distribution.

*Discussion* In this article we demonstrate that bacterial surface rheotaxis can be categorised in four regimes, separated by shear-regulated transitions. A comprehensive model delineates these dynamics and predicts the corresponding critical shear rates. Perhaps surprisingly, the chiral term [Eq. 5] only plays a minor role compared to bacterial rheotaxis in the bulk [8], but the small bias it generates is additive over time and also affects the orientation distribution of bacteria entering the surface in favour of swimming to the right. Oscillations at the surface increase the probability to detach, thus tuning  $\dot{\gamma}_{c2}$  could modify the average residence time and the ability for cells to initiate biofilms. Together, these results shed new light on bacterial transport and allow the development of strategies for controlling surface rheotaxis.

## ACKNOWLEDGMENTS

We are grateful to the authors of Ref. [8], and in particular to Henry Fu, providing the MATHEMATICA notebook including the resistive force theory calculations for a helix subjected to shear flow. We thank Angela Dawson and Vincent Martinez for providing the AB1157 *E. coli* strain. AM acknowledges funding from the Human Frontier Science Program (Fellowship LT001670/2017). EC, NFM, AL, GM acknowledge funding from the ANR-15-CE30-0013 BacFlow. AL and NFM acknowledge funding from the ERC Consolidator Grant PaDyFlow (Agreement 682367). AZ acknowledges funding from the European Union’s Horizon 2020 research and innovation programme under the Marie Skłodowska-Curie grant

(Agreement 653284).

---

- [1] C. Bechinger, R. Di Leonardo, H. Löwen, C. Reichhardt, G. Volpe, and G. Volpe, *Rev. Mod. Phys.* **88**, 045006 (2016).
- [2] A. Zöttl and H. Stark, *J. Phys. Condens. Matt.* **28**, 253001 (2016).
- [3] A. J. T. M. Mathijssen, R. Jeanneret, and M. Polin, Accepted in *Phys. Rev. Fluids* (2018), arXiv:1704.05264.
- [4] J. O. Kessler, *Nature* **313**, 218 (1985).
- [5] W. M. Durham, J. O. Kessler, and R. Stocker, *Science* **323**, 1067 (2009).
- [6] R. Rusconi, J. S. Guasto, and R. Stocker, *Nat. Physics* 10.1038/NPHYS2883.
- [7] M. T. Barry, R. Rusconi, J. S. Guasto, and R. Stocker, *J. Roy. Soc. Interface* **12**, 20150791 (2015).
- [8] Marcos, H. C. Fu, T. R. Powers, and R. Stocker, *Proc. Nat. Acad. Sci.* **109**, 4780 (2012).
- [9] X. Garcia, S. Rafai, P. Peyla, and S. Raza, *Phys. Rev. Lett.* **110**, 138106 (2013).
- [10] A. Hope, O. A. Croze, W. C. K. Poon, M. A. Bees, and M. D. Haw, *Phys. Rev. Fluids* **051201**, 2 (2016).
- [11] B. Ezhilan and D. Saintillan, *J. Fluid. Mech.* , 482 (2015).
- [12] A. Zöttl and H. Stark, *Eur. Phys. J. E* **36**, 9817 (2013).
- [13] A. Zöttl and H. Stark, *Phys. Rev. Lett.* **108**, 218104 (2012).
- [14] Marcos, H. Fu, T. Powers, and R. Stocker, *Phys. Rev. Lett.* **102**, 158103 (2009).
- [15] M. Molaei, M. Barry, R. Stocker, and J. Sheng, *Phys. Rev. Lett.* **113**, 068103 (2014).
- [16] H. Shum and E. A. Gaffney, *Phys. Rev. E* **92**, 063016 (2015).
- [17] O. Sipos, K. Nagy, R. Di Leonardo, and P. Galajda, *Phys. Rev. Lett.* **114**, 258104 (2015).
- [18] A. J. T. M. Mathijssen, A. Doostmohammadi, J. M. Yeomans, and T. N. Shendruk, *J. Fluid Mech.* **806**, 35 (2016).
- [19] Rothschild, *Nature* **198**, 1221 (1963).
- [20] A. Berke, L. Turner, H. Berg, and E. Lauga, *Phys. Rev. Lett.* **101**, 038102 (2008).
- [21] G. Li and J. X. Tang, *Phys. Rev. Lett.* **103**, 078101 (2009).
- [22] G. E. Ward, C. J. Brokaw, D. L. Garbers, and V. D. Vacquier, *J. Cell Biol.* **101**, 2324 (1985).
- [23] H. C. Berg and L. Turner, *Biophys. J.* **58**, 919 (1990).

- [24] W. R. DiLuzio, L. Turner, M. Mayer, P. Garstecki, D. B. Weibel, H. C. Berg, and G. M. Whitesides, *Nature* **435**, 1271 (2005).
- [25] R. W. Nash, R. Adhikari, J. Tailleur, and M. E. Cates, *Phys. Rev. Lett.* **258101**, 258101 (2010).
- [26] A. Costanzo, R. Di Leonardo, G. Ruocco, and L. Angelani, *J. Phys. Condens. Matt.* **24**, 065101 (2012).
- [27] W. E. Uspal, M. N. Popescu, S. Dietrich, and M. Tasinkevych, *Soft Matter* **11**, 434 (2015).
- [28] J. Palacci, S. Sacanna, A. Abramian, J. Barral, K. Hanson, A. Y. Grosberg, D. J. Pine, and P. M. Chaikin, *Science Advances* **1**, e1400214 (2015).
- [29] V. Kantsler, J. Dunkel, M. Blayney, and R. E. Goldstein, *eLife* , 02403 (2014).
- [30] C. K. Tung, F. Ardon, A. Roy, D. L. Koch, S. S. Suarez, and M. Wu, *Phys. Rev. Lett.* **114**, 108102 (2015).
- [31] T. Kaya and H. Koser, *Biophys. J.* **102**, 1514 (2012).
- [32] J. Hill, O. Kalkanci, J. McMurry, and H. Koser, *Phys. Rev. Lett.* **98**, 068101 (2007).
- [33] N. Figueroa-Morales, G. Leonardo Miño, A. Rivera, R. Caballero, E. Clément, E. Altshuler, and A. Lindner, *Soft Matter* **11**, 6284 (2015).
- [34] E. Altshuler, G. Miño, C. Pérez-Penichet, L. D. Río, A. Lindner, A. Rousselet, and E. Clément, *Soft Matter* **9**, 1864 (2013).
- [35] R. Bretherton, *Proc. Roy. Soc.* **153**, 953 (1961).
- [36] See Supplementary Information at [URL to be inserted by publisher]..
- [37] T. Darnige, N. Figueroa-Morales, P. Bohec, A. Lindner, and E. Clément, *Rev. Sci. Instr.* **88**, 055106 (2017).
- [38] S. E. Spagnolie and E. Lauga, *J. Fluid. Mech.* **700**, 105 (2012).
- [39] E. Lauga, W. R. DiLuzio, G. M. Whitesides, and H. a. Stone, *Biophys. J.* **90**, 400 (2006).
- [40] G. Li, L.-K. Tam, and J. X. Tang, *Proc. Nat. Acad. Sci.* **105**, 18355 (2008).
- [41] J. Dunstan, G. Mino, E. Clement, and R. Soto, *Phys. Fluids* **24**, 011901 (2012).
- [42] S. Bianchi, F. Saglimbeni, and R. Di Leonardo, *Phys. Rev. X* **7**, 011010 (2017).
- [43] T. Kaya and H. Koser, *Phys. Rev. Lett.* **103**, 138103 (2009).
- [44] G. B. Jeffery, *Proc. Roy. Soc. A* **102**, 161 (1922).
- [45] C. Pozrikidis, *J. Fluid. Mech.* **541**, 105 (2005).
- [46] M. Makino and M. Doi, *Phys. Fluids* **17** (2005), 10.1063/1.2107867.

- [47] K. Miki and D. E. Clapham, Curr. Biol. **23**, 443 (2013).
- [48] K. Drescher, J. Dunkel, L. H. Cisneros, S. Ganguly, and R. E. Goldstein, Proc. Nat. Acad. Sci. **108**, 10940 (2011).
- [49] K. Schaar, A. Zöttl, and H. Stark, Phys. Rev. Lett. **115**, 038101 (2015).
- [50] A. J. T. M. Mathijssen, A. Doostmohammadi, J. M. Yeomans, and T. N. Shendruk, J. Roy. Soc. Interface **13**, 20150936 (2016).
- [51] J. Schwarz-Linek, J. Arlt, A. Jepson, A. Dawson, T. Vissers, D. Miroli, T. Pilizota, V. A. Martinez, and W. C. K. Poon, Colloids and Surfaces B: Biointerfaces **137**, 2 (2016).
- [52] M. Raible and A. Engel, Appl. Organometallic Chem. **18**, 536 (2004).
- [53] C. Pozrikidis, J. Fluid. Mech. **541**, 105 (2005).

## Appendix A: Experimental Details

Two complementary types of experimental techniques are used: (1) fluorescently labeling of bacterial flagella to obtain cell orientation and (2) three-dimensional tracking to obtain full information about their trajectories.

### 1. Experimental protocol to obtain bacteria orientations

For flagella visualization, we use a genetically modified strain from the AB1157 wild-type (AD1) published in Ref. [51]. This strain contains a FliC mutation to bind to the dye from Alexa Fluor. Single colonies of frozen stocks are incubated overnight (16 h) in 5mL of liquid Luria Broth at 30 C, shaken for aeration at 200 rpm. The bacteria are washed and resuspended in Bergs motility buffer (BMB: 6.2 mM  $K_2HPO_4$ , 3.8 mM  $KH_2PO_4$ , 67 mM  $NaCl$ , and 0.1 mM  $EDTA$ ). For flagella staining, 0.5 mL of the bacterial suspension in BMB at  $2 \times 10^9 \text{ bact/mL}$  are mixed with 5  $\mu\text{L}$  of Alexa Fluor 546 C5-maleimide suspended at 5mg/mL in DMSO. The sample is kept in the dark, shaking at 100 rpm for 1 h. Bacteria are then three times washed in BMB and finally suspended at  $10^8 \text{ bact/mL}$  in BMB supplemented with polyvinylpyrrolidone (PVP 350 kDa: 0.005%) to prevent sticking to the walls of the microchannel. The solution is then seeded with passive particles to be used for flow velocity determination (latex beads from Beckman Coulter  $d = 2\mu\text{m}$ , density  $\rho = 1.027\text{g/mL}$  at a volume fraction  $\phi = 10^{-7}$ ).

This suspension is perfused through a  $H = 20\mu m$  deep,  $W = 200\mu m$  wide and several millimeters long rectangular microfluidic PDMS channel [see Fig. 1(a) of the main text]. The Poiseuille flow is imposed by height difference between the inlet and outlet reservoirs and vary the wall-shear rate  $0 < \dot{\gamma} < 100s^{-1}$ . We focus on the bottom wall and capture the bacterial dynamics of bacteria within  $5\mu m$  from the surface, using an inverted microscope (Zeiss-Observer, Z1) with a high magnification objective ( $100\times/0.9$  DIC Zeiss EC Epiplan-Neofluar) and a digital camera ANDOR iXon 897 EMCCD at 30fps.

As bacteria are transported downstream, they are kept in the frame of observation by manually displacing the microscope's stage, which position is registered. During post-processing we extract the bacterial positions and orientations from the images and reconstruct the whole trajectories, which extend for as long as  $1mm$ . Oscillation frequencies were obtained by Fourier-transforming the orientation data and extracting the dominant mode.

## 2. Experimental protocol to obtain bacteria trajectories

*Bacteria culture* The bacteria are smooth swimmers *E. coli* (CR20), a mutant strain that almost never tumble. Suspension are prepared using the following protocol: bacteria are inoculated in 5mL of culture medium (M9G) with antibiotics and grown over night. In this way, bacteria with a fluorescently stained body are obtained. Then the bacteria are transferred in Motility Buffer (MB) and supplemented with L-serine and polyvinyl pyrrolidone (PVP). The addition of L-serine increases the bacteria mobility and PVP is classically used to prevent bacteria from sticking to the surfaces. The interactions that come into play using this system are thus solely steric and hydrodynamic. After incubating for an hour in the medium to obtain a maximal activity, the solution was mixed with Percol (1:1) to avoid bacteria sedimentation. Under these conditions, the average swimming speed is  $v_s = 30\mu m/s$ . For the experiments the suspension is diluted strongly such as to be able to observe single bacteria trajectories without interactions between bacteria.

*Microfluidic channel* The experimental cell is a rectangular channel made in PDMS using soft lithography techniques. The channel height is  $h = 100\mu m$ , the width  $w = 600\mu m$  and its length is of several millimeters.

*Experimental protocol and bacterial detection* Using a syringe pump (dosing unit: Low Pressure Syringe Pump neMESYS 290N and base: Module BASE 120N) we flow the sus-

pension inside the channel at different flow rates (1 1,88 4,5 9 18 50 nL.s<sup>-1</sup>), corresponding to wall shear rates of 1-50 s<sup>-1</sup>. To have access to the 3D trajectories of single bacteria under flow we use a 3D Lagrangian tracker [37] which is based on real-time image processing, determining the displacement of a  $xy$  mechanical stage to keep the chosen object at a fixed position in the observation frame. The  $z$  displacement is based on the refocusing of the fluorescent object, keeping the moving object in focus with a precision of a few microns in  $z$ . The acquisition frequency is 30 Hz. The Lagrangian tracker is composed of an inverted microscope (Zeiss-Observer, Z1) with a high magnification objective (100X/0.9 DIC Zeiss EC Epiplan-Neofluar), a  $xy$  mechanically controllable stage with  $z$  piezo-mover from Applied Scientific Instrumentation (ms-2000-flat-top- $xyz$ ) and a digital camera ANDOR iXon 897 EMCCD. Trajectories are only considered when far away from the lateral walls (distances larger than 100  $\mu\text{m}$ ) and as long as they are within 5  $\mu\text{m}$  from the surface. A typical error on this distance, resulting from the uncertainty on the  $z$ -detection as well as the uncertainty on the position of the bottom surface is around 3  $\mu\text{m}$ .

### 3. Data analysis

To determine the frequency of the bacterial oscillations, we Fourier transform the bacterial trajectories obtained from experiments for different shear rates. (1) In the case of the experiments using bacteria with fluorescently labelled flagella, the in-plane angle  $\psi(t)$  of the cell orientation is determined by fitting an ellipse to the acquired camera image and distinguish between head and tail by the velocity director. (2) In the case of the 3D tracking experiments, the orientation cannot be determined in the same manner, but the lateral velocity  $v_z(t)$  is used to search for oscillatory motion. Hence, either  $\psi(t)$  or  $v_z(t)$  are Fourier transformed for trajectories of sufficiently long duration to resolve the lowest and highest frequencies accurately. The frequency of each trajectory is determined by selecting the highest peak in the resulting Fourier spectrum. This is repeated for all trajectories to form an ensemble of frequencies, from which we evaluate the mean frequency  $f(\dot{\gamma})$  and its standard deviation.

## Appendix B: Chirality induced rheotaxis

Marcos et al. used Resistive Force Theory (RFT) to calculate the rheotactic behaviour of helical bacteria in shear flows in the bulk [8, 14]. Based on their work and using their MATHEMATICA notebook, that includes the resistive force theory calculations for a helix subjected to shear flow, we are able to identify the full angular dependence of the rheotactic torque [Eqs. (5) of the main text].

In RFT a helical flagellum segment is approximated by a stiff slender rod with anisotropic friction coefficients  $\xi_{\perp}$  and  $\xi_{\parallel}$  with  $1 < \xi_{\perp}/\xi_{\parallel} < 2$ . The viscous force per unit length opposing the motion of a rod is written as  $\mathbf{f} = -\xi_{\parallel}\mathbf{u}_{\parallel} - \xi_{\perp}\mathbf{u}_{\perp}$ , with the local rod velocity ( $\mathbf{v}_l$ ) relative to the external shear flow ( $\mathbf{v}_f$ ),  $\mathbf{u} = \mathbf{v}_l - \mathbf{v}_f = \mathbf{u}_{\parallel} + \mathbf{u}_{\perp}$  where the local rod velocity  $\mathbf{v}_l$  is a sum of its translational and rotational velocity  $\mathbf{v}_l = \mathbf{v} + \boldsymbol{\Omega} \times \mathbf{r}(s; \psi, \theta)$ , and  $\mathbf{u}_{\parallel} = (\mathbf{u} \cdot \hat{\mathbf{t}})\hat{\mathbf{t}}$ ,  $\mathbf{u}_{\perp} = \mathbf{u} - \mathbf{u}_{\parallel}$ ; here  $\mathbf{r}(s; \psi, \theta)$  is a space-curve of a helix parametrized by  $s$  and oriented along the swimmer direction, given by the angles  $\psi$  and  $\theta$ , and the tangent is  $\hat{\mathbf{t}} = (d\mathbf{r}/ds)/|d\mathbf{r}/ds|$ . After integrating the force and torque on the helix at angles  $\psi$  and  $\theta$  over the full helix length and averaging over the helix phase angle, one can in principle solve for the unknown helix velocity  $\mathbf{v}$  and angular velocity  $\boldsymbol{\Omega}$ . While in a good approximation the helix will rotate in flow similar as a rigid rodlike particle [8], the velocity  $\mathbf{v}$ , which vanishes for non-chiral objects, determines chirality-induced migration velocity.

The analytic expressions for  $\mathbf{v}$  obtained with MATHEMATICA are rather lengthy and cannot be reduced or simplified by the program. However, we can plot the velocity components  $v_x$ ,  $v_y$  and  $v_z$  depending on its orientation angles  $\psi$  and  $\theta$  for a given helix shape in Fig. 5(a-c), respectively. Fortunately, by try and error, we could extract from these figures the angular dependencies of the velocities, which are shown in Fig. 5(d-f), and read

$$v_x^H = -k_1 \dot{\gamma} \sin 2\theta \cos^2 \psi \quad (\text{B1})$$

$$v_y^H = -k_1 \dot{\gamma} \sin \theta \sin 2\psi \quad (\text{B2})$$

$$v_z^H = 2k_1 \dot{\gamma} (-\sin^2 \theta \cos^2 \psi + \cos 2\psi) \quad (\text{B3})$$

which linearly increase with the shear rate  $\dot{\gamma}$ , and where the prefactor  $k_1$  only depends on the helix geometry and is  $k_1 > 0$  for a left-handed helix (as it is the case for the normal form of *E. coli* bacteria), and  $< 0$  otherwise. Hence, for example when a helix is aligned with the flow ( $\theta = 0$ ,  $\psi = 0$ ), the rheotactic drift  $v_z^H = 2k_1 \dot{\gamma} > 0$  is directed “to the left”



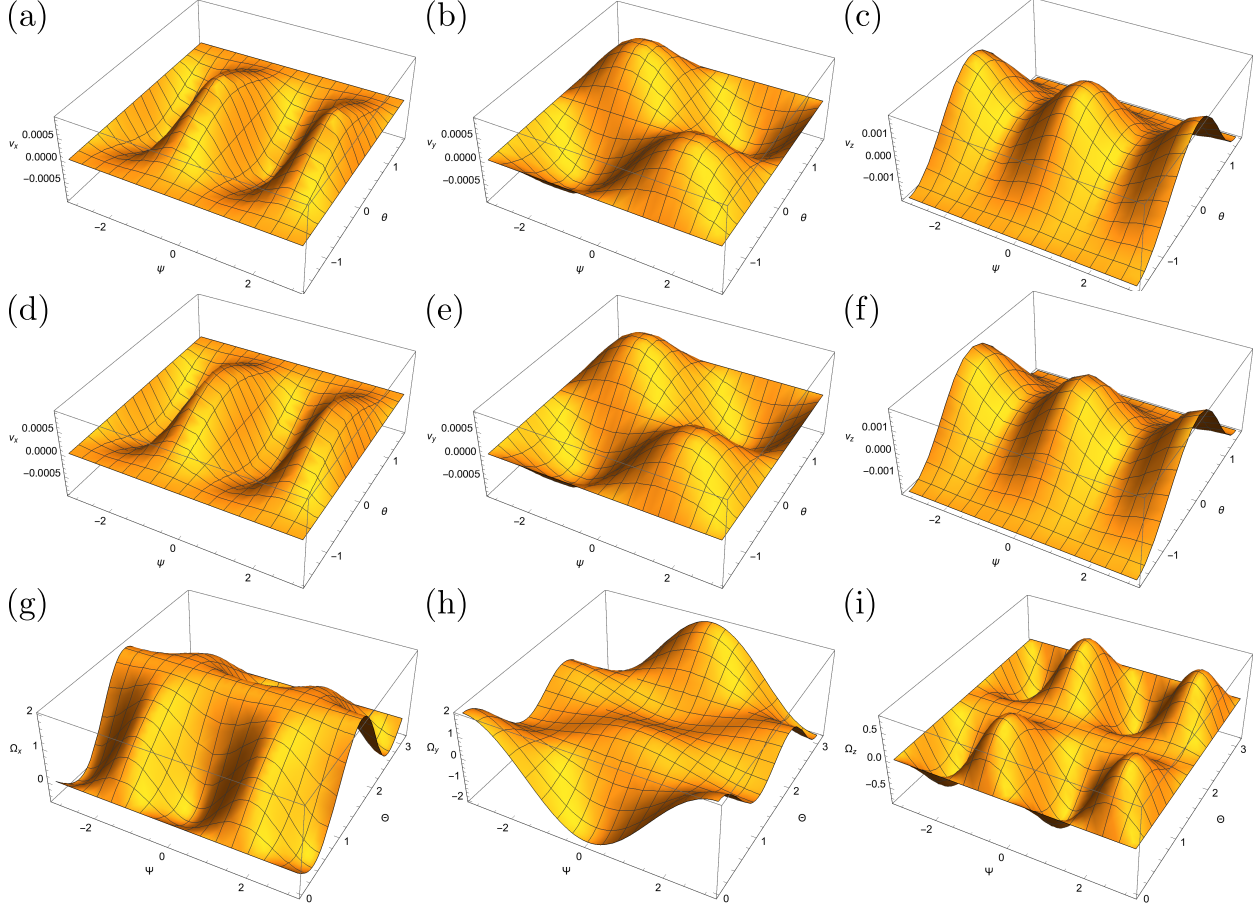


FIG. 5. (a-c)  $x$ ,  $y$ , and  $z$  component of the rheotactic velocities of a helix (graphical solution). We confirm in (d-f) that the curves in (a-c) are given by Eqs. (B1)-(B3). (g-i) Rheotactic angular velocities for a bacterium [Eqs. (B4)-(B6)].

[see Fig. 2(b) in the main text] for left-handed helices [14].

However, swimming bacteria with a left-handed flagellum swim “to the right” [8]. This is explained by the combination of the passive rheotactic drift and the active swimming of the bacterium. The swimmer is oriented along direction  $\mathbf{e} = (-\cos\theta\cos\psi, \sin\theta, -\cos\theta\sin\psi)$ , and a rheotactic torque can be expressed as  $\boldsymbol{\Omega}^H = -k_2\mathbf{e} \times \mathbf{v}$  where the prefactor  $k_2$  depends on the shape of the cell body [8]. The components  $\Omega_x^H$ ,  $\Omega_y^H$  and  $\Omega_z^H$  are shown in Fig. 5(g-i) and read

$$\Omega_x^H = -\bar{\nu}_H \dot{\gamma} (\cos 2\theta - 2 \cos^2 \theta \sin^2 \psi) \quad (\text{B4})$$

$$\Omega_y^H = -\bar{\nu}_H \dot{\gamma} (\cos \theta + \cos 3\theta) \cos \psi / 2 \quad (\text{B5})$$

$$\Omega_z^H = -\bar{\nu}_H \dot{\gamma} \cos^2 \theta \sin \theta \sin 2\psi \quad (\text{B6})$$

where we used  $\bar{\nu}_H = 2k_1k_2$ . Hence, this torque reorients the flagellum of the bacterium ‘to the left’, after which it will swim ‘to the right’. The components of this torque in the  $\psi$  and  $\theta$  directions are written down in Eq. (5) of the main text.

### Appendix C: Simulations of surface rheotaxis

The bacterial surface rheotaxis is simulated by numerical integration of the orientation dynamics, encapsulated by the covariant Langevin equation [52] written out in terms of the angles  $(\psi, \theta)$  that live on the curved surface  $|\mathbf{p}| = 1$ ,

$$\psi(t + \delta t) - \psi(t) = \delta t(\Omega_\psi^W + \Omega_\psi^J + \Omega_\psi^H + \Omega_\psi^V) + \frac{\sqrt{2D_r\delta t}}{\cos \theta} \eta_\psi, \quad (\text{C1})$$

$$\theta(t + \delta t) - \theta(t) = \delta t(\Omega_\theta^W + \Omega_\theta^J + \Omega_\theta^H + \Omega_\theta^V) - \tan(\theta)D_r\delta t + \sqrt{2D_r\delta t} \eta_\theta, \quad (\text{C2})$$

where  $D_r = 0.057\mu\text{m}^2/\text{s}$  is the rotational diffusion coefficient [48], the noise correlations are defined as  $\langle \eta_i \rangle = 0$  and  $\langle \eta_i(t)\eta_j(t') \rangle = \delta_{ij}\delta(t - t')$  and the deterministic terms are written out explicitly in equations (E1-E2) below.

At the start of a trajectory, the swimmer reaches the surface with a small negative dipping angle,  $\theta(0) = -\pi/10$ , and a random uniformly distributed in-plane angle,  $\psi(0) \in [-\pi, \pi]$ . Subsequently, its orientation  $(\psi(t), \theta(t))$  is integrated using a forward Euler scheme with time step  $\delta t = 10^{-3}\text{s}$ , and after every time step the orientation angles are renormalised to their domains,  $\psi \in [-\pi, \pi]$  and  $\theta \in [-\pi/2, \pi/2]$ , by setting

$$\psi \rightarrow \text{mod}(\psi, 2\pi, -\pi), \quad (\text{C3})$$

$$\theta \rightarrow \text{abs}(\theta + \pi/2) - \pi/2. \quad (\text{C4})$$

Next, the spatial dynamics is obtained by computing the velocity parallel to the wall,

$$\mathbf{v}_{||} = v_0\mathbf{p}_{||} + \dot{\gamma}\delta\hat{\mathbf{x}}, \quad (\text{C5})$$

where  $v_0 = 20\mu\text{m}/\text{s}$  is the swimming speed,  $\mathbf{p}_{||} = p_x\hat{\mathbf{x}} + p_z\hat{\mathbf{z}} = (-\cos\theta\cos\psi, -\cos\theta\sin\psi)$  is the swimmer orientation parallel to the wall, and  $\delta = W/2 = 0.5\mu\text{m}$  is the distance from the wall. The surface trajectories are then found by numerical integration of  $\dot{\mathbf{r}}_{||} = \mathbf{v}_{||}$ . A trajectory ends when the dipping angle exceeds the escape angle,  $\theta_e = \pi/6$ , after which the swimmer escapes the surface.

Hence,  $N = 10^4$  trajectories are simulated for 10 values of the applied shear rate,  $\dot{\gamma} = 10^{2.5(i-1)/9}$ , where  $i = 1, 2, \dots, 9, 10$ . From these trajectories  $(\psi, \theta)$  the distribution of the in-plane angle,  $\text{PDF}(\psi)$ , follows immediately. To determine the frequency of the bacterial oscillations, a trajectory must be sufficiently long to resolve the smaller frequencies. At high shear the average trajectory (residence) time is smaller than at low shear, so we discard trajectories shorter than 10s, which leaves at least  $\sim 100$  trajectories for any shear rate. The frequencies of the remaining trajectories are then obtained individually by Fourier transforming the in-plane angle  $\psi(t)$ , and selecting the frequency of the highest peak in the resulting Fourier spectrum. Using this ensemble, we evaluate the mean frequency  $f(\dot{\gamma})$  and its standard deviation.

#### Appendix D: Estimation of model parameters

We find that our results are robust w.r.t. changes of the model parameters. The numerical values of the critical shear rates may vary, especially in experiments due to the variability of individual bacteria, but qualitatively speaking the same behaviors (regimes) are always observed. In the following we present the parameters we used to produce Figs. 3 and 4 of the main text.

*a. Swimmer aspect ratio  $\Gamma$ :* While cell bodies of *E. coli* bacteria have typical aspect ratios of  $\Gamma_B \approx 3$ , including the flagella bundle increases the effective aspect ratio  $\Gamma$ . We choose  $\Gamma = 5$  for convenience; note that  $\Gamma$  does not enter the model equations directly, but rather  $G = (\Gamma^2 - 1)/(\Gamma^2 + 1) \lesssim 1$ , which does not change very significantly when increasing  $\Gamma$  further.

*b. Hydrodynamic/steric reorientation frequency at wall  $\nu_W$ :* Steric reorientation rates have been reported to be of the order  $\nu_W^{\text{steric}} \sim 1 - 10 \text{ s}^{-1}$  for flagellated *Caulobacter* bacteria [21]. Reorientation rates away from the walls due to hydrodynamic interactions can be approximated by far-field expressions [38] (see Eq. (2) in main text) with a prefactor  $\nu_W^{HI} = 3p/(128\pi\eta h^3)$ , where  $p = 0.8pN \mu\text{m}$  is the dipole strength of *E. coli* bacteria [48],  $\eta = 10^{-3} \text{ Pa s}$  the viscosity of water, and  $h$  the distance of the swimmer from the surface. If far-field hydrodynamics would still hold close to the wall ( $h \approx 1 - 2 \mu\text{m}$ ), one would find  $\nu_W^{HI} \approx 0.75 - 6 \text{ s}^{-1}$ , which is smaller than the steric contribution but also acts when the swimmer moves away from the surface, so it could increase the wall residence time [49]. Also

note that the  $1/h^3$  dependence likely gives an overestimate when a swimmer is very close to the wall,  $h < 1\mu\text{m}$ , as the multipole approximation breaks down. Taking this information together, we use  $\nu_W = 3s^{-1}$  to capture the combined effects of steric and hydrodynamic interactions.

*c. Circling frequency near a wall  $\nu_C$ :* The typical circling frequencies of an *E. coli* bacterium close to a boundary is on the order of  $\sim 1\text{s}$  [39]. Since the frequency  $\Omega_\psi^W \approx 2\nu_C$  for  $G \sim 1$  [see Eqn. (3) of the text], we chose  $\nu_c = 0.5s^{-1}$ , which gives typical circles of radius  $R = v_0/\Omega_\psi^W \sim 20\mu\text{m}$ . Note that there is quite a variety in these frequencies between different individual bacteria [39, 40], which will lead to bacteria having different individual critical shear rates.

*d. Chirality-induced bulk reorientation rate  $\bar{\nu}_H$ :* The rheotactic drift for bacteria in bulk has been quantified by Marcos et al. [8, 14], as described in §II above. We expect similar rheotactic strength for our bacteria, which is satisfied approximately for  $\bar{\nu}_H = 0.02$ . Because this term is significantly smaller than the other contributions, we find that variations in  $\bar{\nu}_H$  do not affect the model results significantly.

*e. Jeffery orientation rates:* We assume that the Jeffery rotation frequency is not modified significantly close to the wall, in accordance with simulations of freely suspended ellipsoids near a boundary [53].

*f. Anchoring reorientation rate  $\bar{\nu}_V$ :* Due to a similar size of the head, we expect that the order of magnitude for a bacterium is comparable to the values found for sperm cells [30], and we chose  $\bar{\nu}_V = 0.75$ . Note, the magnitude of this effect is reduced strongly when the swimmer is not in close proximity to the walls, since it relies on enhanced friction obtained from the lubrication regime [30]. When the swimmer is oriented away from the surface ( $\theta > 0$ ) we expect this effect to vanish quickly, quantified by a small value  $\theta_V = 0.04$  used in the tanh-function [see Eq. (6)].

*g. Escape angle  $\theta_e$ :* In order to determine when a swimmer leaves a surface, it has to reach a certain escape angle  $\theta_e$  which we chose to be  $\theta_e = \pi/6$ , following references [48–50]. Note that  $\theta_e$  does not influence the dynamics in the model per se, but rather defines how long a bacterium stays at a surface.

TABLE I. Summary of model parameters

Name	Symbol	Value	Units
Bacterial aspect ratio	$\Gamma$	5	
Wall alignment rate	$\nu_W$	3	$\text{s}^{-1}$
Circle swimming frequency	$\nu_D$	0.5	$\text{s}^{-1}$
Helix rheotactic torque strength	$\bar{\nu}_H$	0.02	
Weathervane effect strength	$\bar{\nu}_V$	0.75	
Weathervane effect angle	$\theta_V$	0.04	rad
Wall escape angle	$\theta_e$	$\pi/6$	
Swimming speed at wall	$v_s$	20	$\mu\text{ms}^{-1}$
Swimming height from wall	$h_s$	0.5	$\mu$
Rotational noise coefficient	$D_r$	0.057	$\text{s}^{-1}$

## Appendix E: Model Fixed points and frequencies

### 1. Approximation of the Equilibrium Rheotactic Orientations

Combining the deterministic contributions of our rheotactic model, we have

$$\begin{aligned}
 \Omega_\psi = & \nu_C(1 - 3\sin^2\theta + G\cos^2\theta(1 + 3\sin^2\theta)) \\
 & + \frac{\dot{\gamma}\nu_J}{2}(1 + G)\sin\psi\tan\theta \\
 & + \dot{\gamma}\bar{\nu}_H\cos\psi\frac{\cos 2\theta}{\cos\theta} \\
 & - \dot{\gamma}\bar{\nu}_V\sin\psi\left(\frac{1}{2}\left(1 - \tanh\frac{\theta}{\theta_V}\right)\right), \tag{E1}
 \end{aligned}$$

$$\begin{aligned}
 \Omega_\theta = & -\nu_W\sin 2\theta\left(1 + \frac{G}{2}(1 + \cos^2\theta)\right) \\
 & + \frac{\dot{\gamma}\nu_J}{2}\dot{\gamma}(1 - G\cos 2\theta)\cos\psi \\
 & + \dot{\gamma}\bar{\nu}_H\sin\psi\sin\theta \\
 & - \dot{\gamma}\bar{\nu}_V\sin\theta\left(\frac{1}{2}\left(1 - \tanh\frac{\theta}{\theta_V}\right)\right). \tag{E2}
 \end{aligned}$$

## 2. Adler Transition from Circling to Straight Motion

The first transition, from circling to straight motion, has previously been described in the literature for sperm cells [30]. It can be characterised as the point at which the upstream-directed torque from weathervane effect becomes more important than the constant torque from the bacterial circling on surfaces. This can be captured in the limit of small dipping angles,  $\theta \rightarrow 0$ , where the one-dimensional equation for the in-plane angle (E1) simplifies to

$$\Omega_\psi = \nu_C(1 + G) - \frac{1}{2}\dot{\gamma}\bar{\nu}_V \sin \psi + \dot{\gamma}\bar{\nu}_H \cos \psi. \quad (\text{E3})$$

This can immediately be solved for the equilibrium angle  $\psi_0$  where  $\Omega_\psi = 0$ . The solution is a little long to write down, but is nothing more than an arctangent. Further progress can be made by noting that  $\bar{\nu}_H \ll \bar{\nu}_V$  and also  $\cos \psi \ll \sin \psi$ , near  $\psi \sim \pi/2$ , at shear rates close to the transition where the bacteria swim to the right. Consequently, the resulting equilibrium angle is given by

$$\psi_0 = \arcsin \frac{2(1 + G)\nu_C}{\bar{\nu}_V \dot{\gamma}}. \quad (\text{E4})$$

This function has no real solutions for shear rates smaller than a critical value. Indeed, the rotating bacteria do not have a stable equilibrium orientation, but for large enough shear they break out of their circles and maintain a constant bearing. Therefore, we found the critical shear rate of Adler transition,

$$\dot{\gamma}_A = \frac{2(1 + G)\nu_C}{\bar{\nu}_V}. \quad (\text{E5})$$

## 3. Approximation of the Equilibrium Rheotactic Orientations

In order to estimate the equilibrium rheotactic orientations at higher shear rates above the Adler transition, the one-dimensional approach breaks down because the dipping angle  $\theta$  becomes significant. This shortcoming is also observed from the 1D solution (E4) that only decreases with increasing shear but does not capture the later increase, which gives rise to an optimum shear rate for upstream swimming.

Therefore, we aim to solve for both  $\psi_0$  and  $\theta_0$  such that  $\Omega_\psi = \Omega_\theta = 0$ . Because it is known that the bacteria swim to the right and left at high shear rates, we linearise equations (E1)

and (E2) about these directions and also consider small dipping angles parallel to the surface:

$$(\psi, \theta) = \left( \alpha \pm \frac{\pi}{2}, \beta \right), \quad (\text{E6})$$

where  $\alpha, \beta \ll 1$ . To first order in  $\alpha$  and  $\beta$ , that yields the linear expression

$$\begin{aligned} \begin{bmatrix} \Omega_\psi \\ \Omega_\theta \end{bmatrix} &= \begin{bmatrix} \nu_W(1+G) \mp \frac{1}{2}\bar{\nu}_V\dot{\gamma} \\ 0 \end{bmatrix} \\ &+ \begin{bmatrix} \mp\bar{\nu}_H\dot{\gamma} & \pm\frac{1}{2}\nu_J\dot{\gamma}(1+G) \pm \frac{\bar{\nu}_V\dot{\gamma}}{2\theta_V} \\ \mp\frac{1}{2}\nu_J\dot{\gamma}(1-G) & -2\nu_W(1+G) - \frac{1}{2}\bar{\nu}_V\dot{\gamma} \pm \bar{\nu}_H\dot{\gamma} \end{bmatrix} \begin{bmatrix} \alpha \\ \beta \end{bmatrix}. \end{aligned} \quad (\text{E7})$$

This matrix equation can be inverted directly: Using the short-hand notation

$$\begin{bmatrix} 0 \\ 0 \end{bmatrix} = \begin{bmatrix} E \\ 0 \end{bmatrix} + \begin{bmatrix} A & B \\ C & D \end{bmatrix} \begin{bmatrix} \alpha \\ \beta \end{bmatrix}, \quad (\text{E8})$$

where  $(A, B, C, D, E)$  are all linear functions of the shear rate  $\dot{\gamma}$ , one obtains the equilibrium in-plane angle

$$\psi_0 = \frac{DE}{BC - AD} \pm \frac{\pi}{2}, \quad (\text{E9})$$

and the equilibrium dipping angle

$$\theta_0 = \frac{CE}{AD - BC}, \quad (\text{E10})$$

with, for completeness,

$$A = \mp\bar{\nu}_H\dot{\gamma} \quad (\text{E11})$$

$$B = \pm\frac{1}{2}\nu_J\dot{\gamma}(1+G) \pm \frac{\bar{\nu}_V\dot{\gamma}}{2\theta_V} \quad (\text{E12})$$

$$C = \mp\frac{1}{2}\nu_J\dot{\gamma}(1-G) \quad (\text{E13})$$

$$D = -2\nu_W(1+G) - \frac{1}{2}\bar{\nu}_V\dot{\gamma} \pm \bar{\nu}_H\dot{\gamma} \quad (\text{E14})$$

$$E = \nu_W(1+G) \mp \frac{1}{2}\bar{\nu}_V\dot{\gamma}. \quad (\text{E15})$$

These results are shown as the dotted lines in Figure 4(b,c) of the main text.

#### 4. Optimal Shear Rate for Upstream Swimming

Continuing from the above theory, it is also possible to extract an estimate for the optimal shear rate for upstream swimming. This occurs when the right equilibrium in-plane angle (given by Eqn. E9 with the top of the  $\pm$  signs, and the green lines in Fig. 4b) is closest to the upstream orientation ( $\psi \rightarrow 0$ ), thus at the minimum with respect to the shear rate. Hence, we seek to solve for

$$0 = \frac{\partial}{\partial \dot{\gamma}} \left[ \frac{(d_0 + d_1 \dot{\gamma})(e_0 + e_1 \dot{\gamma})}{(b_1 \dot{\gamma})(c_1 \dot{\gamma}) - (a_1 \dot{\gamma})(d_0 + d_1 \dot{\gamma})} \right], \quad (\text{E16})$$

where we wrote  $D = d_0 + d_1 \dot{\gamma}$ , and similar for the other functions. This readily gives

$$\dot{\gamma}_+ = \frac{a_1 d_0^2 e_0}{d_0 e_0 (b_1 c_1 - a_1 d_1) \pm \sqrt{b_1 c_1 d_0^2 e_0 (a_1 (d_0 e_1 - d_1 e_0) + b_1 c_1 e_0)}}. \quad (\text{E17})$$

The negative root is the desired optimum, the best shear rate for upstream swimming. Inserting this value into Eqn. E9 then also gives the most upstream orientation.

#### 5. Oscillation frequency

The equilibrium angles derived above are static (Eqs. E9 and E10), so do not depend explicitly on time, but our experiments show that bacteria can also perform oscillatory trajectories. Here we investigate this dynamic behaviour further, and aim to find an estimate for the oscillation frequency.

We start with a linear stability analysis of the equilibrium orientation angles,

$$(\psi, \theta) = (\psi_0 + \epsilon_\psi, \theta_0 + \epsilon_\theta), \quad (\text{E18})$$

where  $\epsilon_\psi, \epsilon_\theta \ll 1$ . Expanding the equations of motion to first order in  $\epsilon_\psi$  and  $\epsilon_\theta$  again yields

$$\begin{bmatrix} \Omega_\psi \\ \Omega_\theta \end{bmatrix} \approx \begin{bmatrix} \mp \bar{\nu}_H \dot{\gamma} & \pm \frac{1}{2} \nu_J \dot{\gamma} (1 + G) \pm \frac{\bar{\nu}_V \dot{\gamma}}{2\theta_V} \\ \mp \frac{1}{2} \nu_J \dot{\gamma} (1 - G) & -2\nu_W (1 + G) - \frac{1}{2} \bar{\nu}_V \dot{\gamma} \pm \bar{\nu}_H \dot{\gamma} \end{bmatrix} \begin{bmatrix} \epsilon_\psi \\ \epsilon_\theta \end{bmatrix}. \quad (\text{E19})$$

The eigenvalues of this matrix, in terms of  $(A, B, C, D)$  given by Eqs. (E11-E15), are

$$\lambda = \frac{1}{2} \left( A + D \pm \sqrt{(A - D)^2 + 4BC} \right) \quad (\text{E20})$$

The real part of the eigenvalues characterises the stability of the equilibrium orientation. For our model parameters it is always negative for all shear rates (Fig. 6a), indicating a stable equilibrium, because of the surface alignment ( $\nu_W$  term).



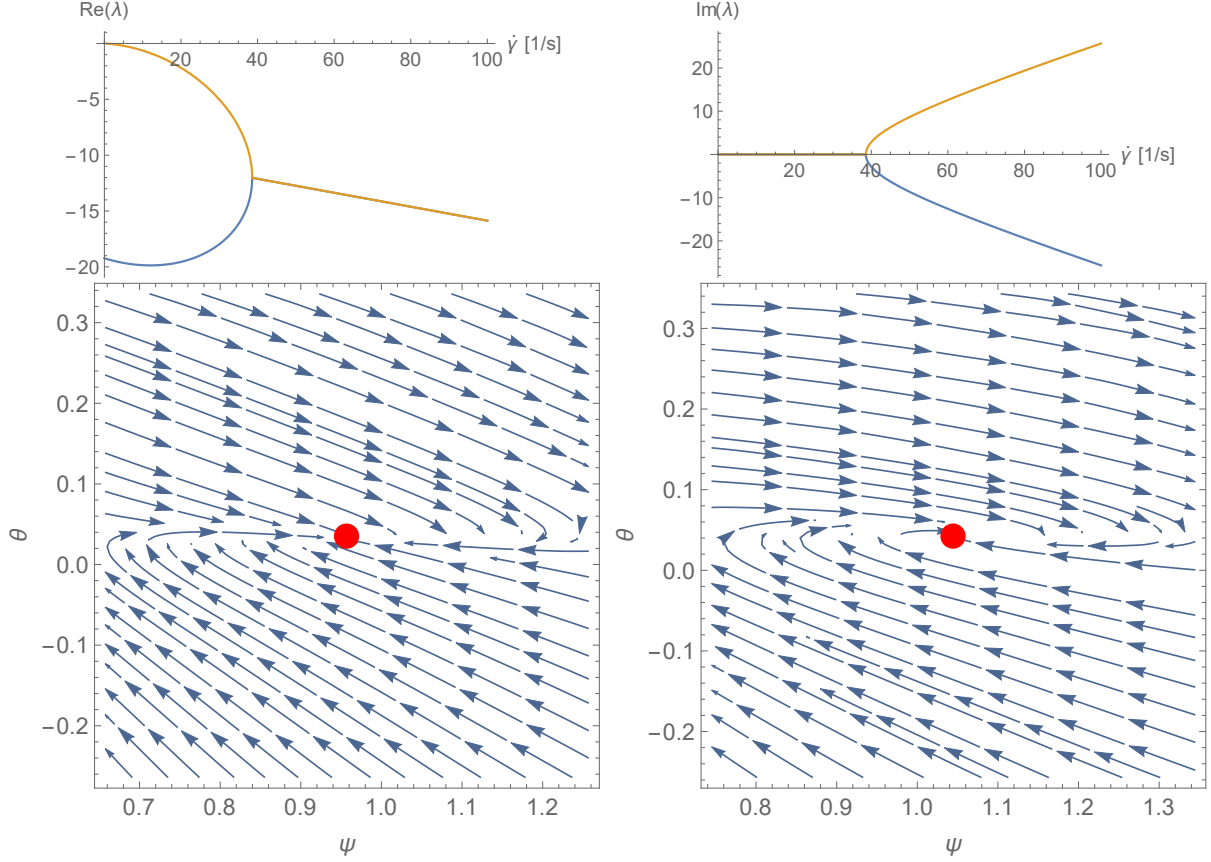


FIG. 6. Emergence of oscillations in the linearised theory, without noise. (a,b) Real and imaginary parts of the eigenvalues (Eqn. E20), characterising fixed point stability and oscillatory motion. The critical shear rate here is  $\dot{\gamma}_O = 38.6\text{s}^{-1}$ . (c,d) Angular dynamics ( $\Omega_\psi, \Omega_\theta$ ) at shear rates  $\dot{\gamma} = 30, 50\text{s}^{-1}$ , respectively, featuring a "star-type" fixed point below  $\dot{\gamma}_O$  and a "spiral-type" fixed point above. Parameters used are ( $\Gamma = 5$ ,  $\nu_W = 5\text{s}^{-1}$ ,  $\nu_C = 0.5\text{s}^{-1}$ ,  $\bar{\nu}_H = 0.02\text{s}^{-1}$ ,  $\bar{\nu}_V = 0.25\text{s}^{-1}$ ,  $\theta_V = 0.1$ ), and shown is the right-oriented swimming direction,  $\psi = \alpha + \pi/2$  in Eqn. E6.

The imaginary part, however, characterises the presence of oscillations. For small shear rates the imaginary part is zero, but above a certain shear rate oscillations emerge (Fig. 6b). This occurs when  $(A - D)^2 = 4BC$ , at the critical shear rate

$$\dot{\gamma}_O = \frac{4(1 + G)\nu_W}{2\sqrt{(1 - G^2) + (1 - G)\bar{\nu}_V/\theta_V} - \bar{\nu}_V \mp 4\bar{\nu}_H}. \quad (\text{E21})$$

Below this shear rate value, the equilibrium orientation is a "star-type" stable fixed point, whereas above  $\dot{\gamma}_O$  it is a "spiral-type" stable fixed point with damped oscillations (Fig. 6c-d).

The oscillation frequency is given directly by the imaginary part of the eigenvalues (Eqn. E20). For high shear rates, this tends to the linear function for the oscillation fre-

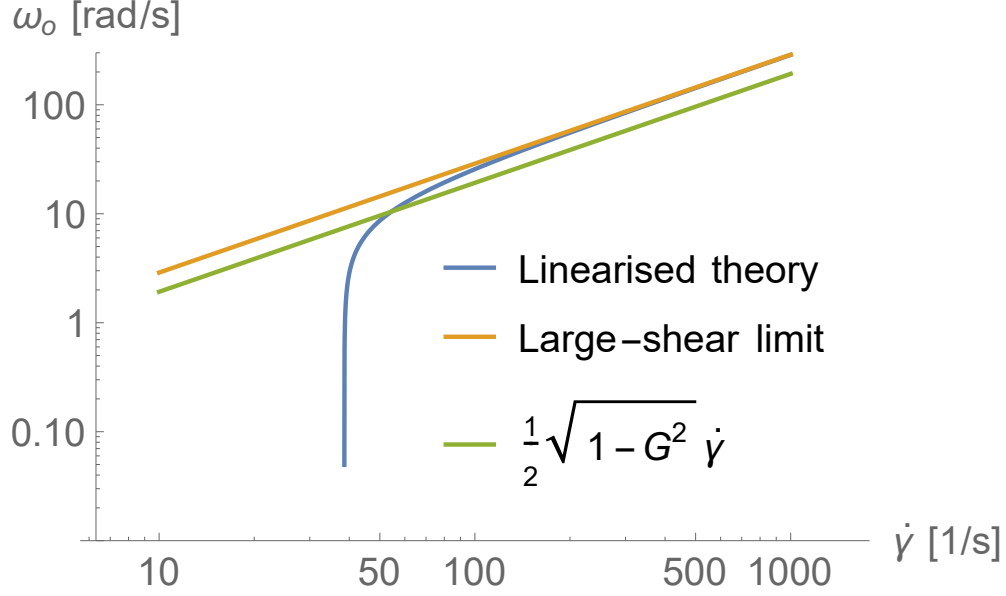


FIG. 7. Oscillation frequency as a function of shear rate. Same parameters as in Fig. 6.

quency

$$\omega_O = \frac{1}{4}\dot{\gamma}\sqrt{4(1 - G^2) + 4(1 - G)\frac{\bar{\nu}_V}{\theta_V} - \bar{\nu}_V^2 \pm 8\bar{\nu}_H\bar{\nu}_V - 16\bar{\nu}_H^2}. \quad (\text{E22})$$

If the weathervane and helix coefficients are small, this simplifies to the frequency

$$\omega_O = \frac{1}{2}\dot{\gamma}\sqrt{(1 - G^2)}. \quad (\text{E23})$$

These results are compared in Fig. 7.

Finally, note that with the presence of noise the bacterium can escape from the equilibrium orientation. This leads to a finite average oscillation amplitude, despite the stability of the fixed point, analogous to a damped harmonic oscillator in contact with a heat reservoir. Bacterial tumble events can enhance this effect and lead to clearly observable oscillations.